

Three-dimensional stacking of canted antiferromagnetism and pseudospin current in undoped Sr₂IrO₄: Symmetry analysis and microscopic model realization

Yun-Peng Huang^{1,2,*}, Jin-Wei Dong^{1,2,*}, Ziqiang Wang^{3,†} and Sen Zhou^{1,2,4,‡}

¹CAS Key Laboratory of Theoretical Physics, Institute of Theoretical Physics, Chinese Academy of Sciences, Beijing 100190, China

²School of Physical Sciences, University of Chinese Academy of Sciences, Beijing 100049, China

³Department of Physics, Boston College, Chestnut Hill, Massachusetts 02467, USA

⁴CAS Center for Excellence in Topological Quantum Computation, University of Chinese Academy of Sciences, Beijing 100049, China



(Received 20 July 2021; accepted 18 October 2021; published 27 October 2021)

Recent optical second-harmonic generation experiments observed unexpected broken spatial symmetries in the undoped spin-orbit Mott insulator Sr₂IrO₄, leading to intensive debates on the nature of its ground state. We propose that it is a canted antiferromagnetism (CAF) with a hidden order of circulating staggered pseudospin current. Symmetry analysis shows that a proper *c*-axis stacking of the CAF and the pseudospin current lead to a magnetoelectric coexistence state that breaks the twofold rotation, inversion, and time-reversal symmetries, consistent with experimental observations. We construct a three-dimensional Hubbard model with spin-orbit coupling and structural distortion for the five localized 5*d* Wannier orbitals centered at Ir sites and demonstrate the microscopic realization of the desired coexistence state in a wide range of band parameters via a combination of self-consistent Hartree-Fock and variational calculations.

DOI: [10.1103/PhysRevB.104.165145](https://doi.org/10.1103/PhysRevB.104.165145)

I. INTRODUCTION

The layered square-lattice iridate Sr₂IrO₄ has been intensively studied since the discovery of the spin-orbit Mott state [1,2], as a consequence of the interplay between spin-orbit coupling (SOC) and electron correlation [3–9]. The strong SOC of Ir atoms splits the *t*_{2*g*} orbitals into a fully occupied $J_{\text{eff}} = \frac{3}{2}$ quartet and a half-filled $J_{\text{eff}} = \frac{1}{2}$ doublet. The latter is then localized by an otherwise moderate electronic correlation, realizing a single-band pseudospin- $\frac{1}{2}$ Heisenberg antiferromagnet (AFM) on the quasi-two-dimensional (quasi-2D) square lattice [1], with strong exchange couplings $J \sim 60$ meV [10]. This makes Sr₂IrO₄ a promising analog of the cuprates and is thus expected to be another platform for unconventional superconductivity [11–14]. A remarkable range of cuprate phenomenology has been observed in both electron- and hole-doped Sr₂IrO₄, including Fermi surface pockets [15], Fermi arcs [16], pseudogaps [17,18], and *d*-wave gaps [19,20]. Whether a superconducting state exists as in the cuprates requires understanding thoroughly the correlated spin-orbit entangled electronic states observed in Sr₂IrO₄.

The ground state of the undoped Sr₂IrO₄ is of particular interest since it is the parent phase from which these spin-orbit entangled correlated states emerge. The electron correlation in the spin-orbit Mott state results in an insulating ground state with AFM long-range order. Neutron and resonant x-ray measurements reveal that the magnetic moments are aligned

in the basal *ab* plane, with their directions tracking the $\theta \simeq 11^\circ$ staggered IrO₆ octahedra rotation about the *c* axis due to strong SOC [21–25]. This gives rise to a net ferromagnetic (FM) moment along the *a* axis, in addition to the AFM component along the *b* axis. The magnetic structure in a IrO₂ layer is depicted schematically in Fig. 1(a). The net FM moment of each layer is shown to order in a $+ - - +$ pattern along the *c* axis [2,26], where \pm refers to the direction of the FM moment along the *a* axis in each of the four IrO₂ planes in a unit cell. This magnetic ground state, hereinafter denoted as $+ - - +$ canted AFM (CAF), belongs to a centrosymmetric orthorhombic magnetic point group $2/m1'$ with spatial C_{2z} rotation, inversion, and time-reversal symmetries [27]. Recent optical second-harmonic generation (SHG) experiments [27], however, reported evidence of unexpected breaking of spatial rotation and inversion symmetries, pointing to the existence of a symmetry-breaking hidden order. It is argued that the broken symmetries can be caused by loop currents [27–30] which were proposed to account for the pseudogap physics in the high-*T*_c cuprates [31–33]. However, the oxygen 2*p* states in Sr₂IrO₄ are much further away from (~ 3 eV below) the Fermi level than those in the cuprates [1,34], making it disadvantageous to develop the loop currents that requires low-energy oxygen 2*p* states. Furthermore, the experimental measurements [27–30] suggest a magnetoelectric loop-current order that is ferrocially stacked along the *c* axis, which is incompatible with the recent observation [35] of a SHG signal that switches sign every two layers.

On the other hand, a different hidden order, the *d*-wave pseudospin current order (*d*PSCO), has been proposed to describe the band dispersion and the pseudogap phenomena observed in the electron-doped Sr₂IrO₄ [36]. The *d*PSCO state generates circulating staggered pseudospin current with pseudospin-up electrons circulating in one direction and

*These authors contributed equally to this work.

†Corresponding author: wangzi@bc.edu

‡Corresponding author: zhouzen@itp.ac.cn

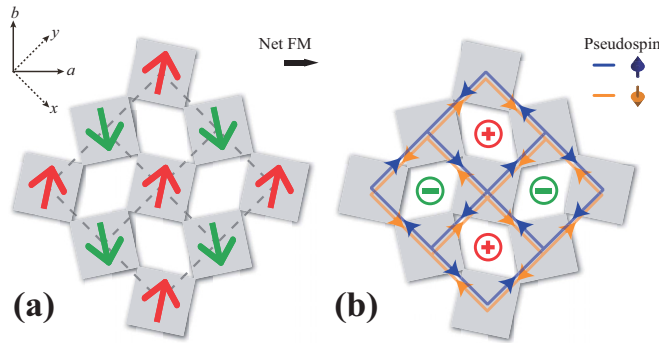


FIG. 1. Schematic topview of (a) the canted antiferromagnet (CAF) and (b) the d -wave pseudospin current order (d PSCO) state in a single IrO_2 plane. Shaded squares represent IrO_6 octahedra, whose staggered rotation about the c axis results in, structurally, two kinds of Ir sites and two kinds of Ir plaquettes. The red and green arrows in (a) denote the magnetic moments on these two kinds of Ir sites. The canting of the antiferromagnetic (AFM) moments leads to a net ferromagnetic (FM) moment along the $+a$ axis, and consequently, the magnetic structure shown in (a) is defined as $+$ in the layered stacking pattern of the three-dimensional (3D) CAF order. The blue and orange lines with arrows in (b) indicate the moving directions of the pseudospin-up and pseudospin-down electrons, respectively. The opposite motion of the electrons with opposite pseudospins creates circulating pseudospin current and staggered pseudospin flux through each Ir plaquette. The direction of the pseudospin flux through these two kinds of Ir plaquettes is denoted by, respectively, red and green symbols at the plaquette center, with \oplus/\ominus corresponding to $\pm c$ axis. The direction of the pseudospin flux in the plaquette enclosing the red parallelogram is \oplus in the d PSCO shown in (b), which is then defined as \oplus in the layered stacking pattern.

pseudospin-down electrons moving in the opposite direction, as illustrated in Fig. 1(b). This gives rise to a d -wave spin-orbit density wave and produces Fermi pockets and Fermi arcs in the nonmagnetic electron-doped Sr_2IrO_4 , in good agreement with angle-resolved photoemission (ARPES) and scanning tunneling microscopy (STM) measurements [15–17,19]. It was argued that the d PSCO is already present in the insulating magnetic phase of the undoped Sr_2IrO_4 , responsible for the observed splitting of the bands [15] at $(\pi, 0)$ whose twofold degeneracy is otherwise protected by certain lattice symmetries [36–38]. While describing remarkably well the highly unconventional quasiparticle properties observed in both the electron-doped and undoped Sr_2IrO_4 , the d PSCO in Ref. [36] was considered in the 2D limit of a single IrO_2 plane. Further studies on the c -axis stacking of the d PSCO and the magnetic order in realistic three-dimensional (3D) systems are necessary to compare directly with the findings of the nonlinear optical experiments and the interpretation in terms of intracell loop currents.

In this paper, we discuss the symmetry properties of the c -axis stacking of CAF, d PSCO, and their coexistence, and study their microscopic realization in realistic 3D models for undoped Sr_2IrO_4 . The rest of the paper is organized as follows. In Sec. II, we perform symmetry analysis. We find that the particular coexistence state with $+ - - +$ CAF and $\oplus \oplus \ominus \ominus$ d PSCO has the symmetries consistent with experimental observations [27–29] in undoped Sr_2IrO_4 . It

is a magnetoelectric state that breaks the spatial twofold rotation, inversion, and time-reversal symmetries. Considering all five $5d$ orbitals of the Ir atoms, a realistic 3D tight-binding (TB) model including SOC (TB + SOC) is constructed in Sec. III A, which describes faithfully the low-energy band structure of Sr_2IrO_4 with the structural distortion. The Hubbard interactions are introduced in Sec. III B and treated within the Hartree-Fock approximation to account for the effects of electron correlations that generate magnetism spontaneously. We obtain CAF phases with different c -axis stacking patterns self-consistently and compare their energies. The $+ - - +$ CAF revealed in experiments is found to be energetically favored in a wide range of band parameters. In Sec. III C, the hidden d PSCO is considered phenomenologically by including a variational term in the Hamiltonian. We fix the stacking pattern of CAF to be $+ - - +$ and compare the energies of coexistence states with different c -axis stacking of d PSCO. The mostly favorable stacking pattern for d PSCO is found to be indeed the desirable $\oplus \oplus \ominus \ominus$, supporting the abovementioned coexistence state as the ground state of undoped Sr_2IrO_4 , with its symmetries consistent with experimental measurements. Discussions and summaries are presented in Sec. IV.

II. SYMMETRY ANALYSES

To be more precise, we denote the magnetic ground state of undoped Sr_2IrO_4 as $(+ - - +)_a$ CAF, where the subscript a specifies the direction of the net FM moment since, in principle, it can be along either the a or b axis [23,24,39]. Fixing the net FM moment along the $\alpha = \{a, b\}$ axis, there are four possible relative stackings along the c axis of the FM in-plane component of the moment in each of the four IrO_2 planes in a unit cell, *i.e.*, $(+ - - +)_\alpha$, $(+ + - -)_\alpha$, $(+ - + -)_\alpha$, and $(+ + + +)_\alpha$. It is easy to show that there is a one-to-one correspondence between states with a FM moment along the a axis and those with a FM along the b axis by performing a C_{4z} rotation around the c axis and a lattice translation. Explicitly, the $(+ - - +)_a$, $(+ + - -)_a$, $(+ - + -)_a$, and $(+ + + +)_a$ CAF states are equivalent to, respectively, $(+ + - -)_b$, $(+ - - +)_b$, $(+ - + -)_b$, and $(+ + + +)_b$ CAF states. The correspondence shall be verified numerically later in the microscopic model calculations presented in Sec. III B by comparing the state energies. Therefore, without loss generality, we restrict the direction of the FM moments to be along the a axis and drop the subscript for the CAF states in the rest of the paper, unless otherwise noted.

The symmetries of the CAF phases (without d PSCO) with different c -axis stacking are summarized in Table I(a), which gives the lattice translation, if it exists, required for a state to recover itself after a symmetry operation of the magnetic point group $2/m1'$: twofold rotation around the z axis C_{2z} , mirror reflection about the ab plane M_z , inversion I with respect to $(\frac{3}{4}, \frac{1}{2}, \frac{1}{2})$, time-reversal T , $C'_{2z} = TC_{2z}$, $M'_z = TM_z$, and $I' = TI$. The state does not have the corresponding symmetry if it could not recover itself by any lattice translation after a symmetry operation. Note that, because the magnetic moments are aligned in the basal ab plane, without any c -axis component, the time-reversal operator T transforms under the same irreducible representation as

TABLE I. Symmetries of c -axis stacked (a) CAF and (b) d PSCO. The table gives the lattice translation required for a state to recover itself after a symmetry operation of the magnetic space group $2/m1'$. The \times symbol means such a lattice translation does not exist. Translation vector $\tau_x = (\frac{1}{2}, 0, 0)$, $\tau_{yz} = (0, \frac{1}{2}, \frac{1}{2})$, and $\tau_{xyz} = (\frac{1}{2}, \frac{1}{2}, \frac{1}{2})$ in terms of the lattice constant (a, b, c) of the conventional unit cell. Note that the states listed in the last two rows of both (a) and (b) are invariant under a lattice translation of τ_{xyz} ; there are thus two possible lattice translations differed by τ_{xyz} .

| Stacking | C_{2z} | M_z | I | T | C'_{2z} | M'_z | I' |
|---|-----------------|---------------------|-----------------|-----------------|-----------------|---------------------|-----------------|
| (a) Symmetries of c -axis stacked CAF: | | | | | | | |
| $+ - - +$ | τ_{xyz} | τ_{yz} | 0 | τ_{xyz} | 0 | τ_x | τ_{xyz} |
| $+ + - -$ | τ_{xyz} | τ_x | τ_{xyz} | τ_{xyz} | 0 | τ_{yz} | 0 |
| $+ + + +$ | \times | \times | 0, τ_{xyz} | \times | 0, τ_{xyz} | τ_x, τ_{yz} | \times |
| $+ - + -$ | \times | τ_x, τ_{yz} | \times | \times | 0, τ_{xyz} | \times | 0, τ_{xyz} |
| (b) Symmetries of c -axis stacked d PSCO: | | | | | | | |
| $\oplus \ominus \oplus \oplus$ | 0 | τ_x | 0 | 0 | 0 | τ_x | 0 |
| $\oplus \oplus \ominus \ominus$ | 0 | τ_{yz} | τ_{xyz} | 0 | 0 | τ_{yz} | τ_{xyz} |
| $\oplus \oplus \oplus \oplus$ | 0, τ_{xyz} | τ_x, τ_{yz} | 0, τ_{xyz} | 0, τ_{xyz} | 0, τ_{xyz} | τ_x, τ_{yz} | 0, τ_{xyz} |
| $\oplus \ominus \ominus \ominus$ | 0, τ_{xyz} | \times | \times | 0, τ_{xyz} | 0, τ_{xyz} | \times | \times |

C_{2z} , and consequently, the point group symmetry operations C'_{2z} , M'_z , and I' are projected to identity E , I , and M_z , respectively, as shown in Table I(a). The $+ - - +$ and $+ + - -$ CAF states share the same symmetries and belong to the centrosymmetric orthorhombic magnetic point group $2/m1'$. However, they are inequivalent in the presence of in-plane anisotropy [39,40], as will be shown in the microscopic model calculations presented in Sec. III B. The nonmagnetoelectric $+ + + +$ CAF breaks $\{C_{2z}, M_z, T, I'\}$, while the magnetoelectric $+ - + -$ CAF breaks $\{C_{2z}, I, T, M'_z\}$ symmetries. They belong to the magnetic point groups $2'/m'$ and $2'/m$, respectively. It has been argued [41] that both the $+ + + +$ and $+ - + -$ CAFs can potentially explain the SHG experiment [27] without invoking the loop currents, and either of them might have been created by the laser pump used in the experiments. The possibility of laser-induced rearrangement of the magnetic stacking, however, has been ruled out by recent comprehensive measurements [35], which show the magnetic stacking pattern is always $+ - - +$ under the experimental condition before strong external field drives it to be $+ + + +$.

Before performing the symmetry analysis for the c -axis stacked hidden d PSCO, we define first the notation for its stacking pattern. The staggered IrO_6 octahedra rotation about the c axis results in two kinds of Ir sites, enclosed by the octahedrons rotated clockwise and anticlockwise, respectively, as shown in Fig. 1(a). In a similar vein, the staggered rotation of IrO_6 octahedra gives rise to two kinds of Ir plaquettes, with the enclosed unshaded parallelograms stretched along, respectively, the x and the y axes, as illustrated in Fig. 1(b). The circulating pseudospin currents generate staggered pseudospin flux through each Ir plaquette. The direction of the pseudospin flux through these two kinds of Ir plaquettes is denoted by, respectively, red and green symbols at the two different plaquette centers, with \oplus/\ominus corresponding to the $\pm c$ axis. The stacking of the d PSCO is then characterized by the

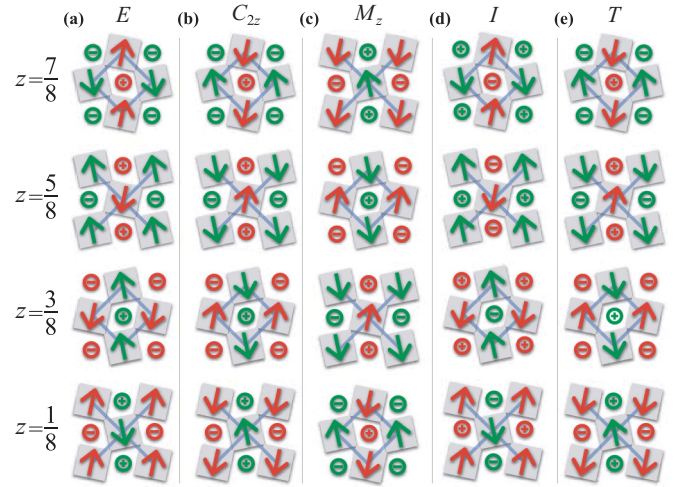


FIG. 2. (a) Structure of Sr_2IrO_4 with $+ - - +$ canted antiferromagnet (AFM) and $\oplus \oplus \oplus \oplus$ d -wave pseudospin current order (d PSCO). Planes through each IrO_2 layer in the unit cell are shown, with z denoting the position of the layer along the c axis. The resultant structure, enclosed in the original unit cell, upon applying the following operations contained within the $2/m1'$ point group: (b) 180° rotation about the c axis, (c) reflection about a mirror plane normal to the c axis, (d) time-reversal, and (e) spatial inversion. Only the structure after mirror reflection can recover the original one by a simple lattice translation.

red symbols in each plane, from top to bottom. For instance, the stacking pattern for the d PSCO shown in Fig. 2(a) corresponds to $\oplus \oplus \ominus \ominus$.

The symmetries of the nonmagnetic phases with possible c -axis stacked d PSCO are summarized in Table I(b). Since the d PSCO is invariant under the time-reversal operator T , any operator is identical to its product with T , e.g., $C_{2z} = C'_{2z}$, $M_z = M'_z$, and $I = I'$. As shown in Table I(b), the $\oplus \ominus \oplus \oplus$, $\oplus \oplus \ominus \ominus$, and $\oplus \oplus \oplus \oplus$ d PSCO states have all the symmetries of the magnetic point group $2/m1'$, while the $\oplus \ominus \oplus \ominus$ d PSCO breaks mirror reflection M_z and inversion I but preserves the symmetries of twofold rotation C_{2z} and time-reversal T . It is important to note that all of the d PSCO states have twofold rotation and time-reversal symmetries. Thus, none of them is able to describe the hidden order in hole-doped $\text{Sr}_2\text{Ir}_{1-x}\text{Rh}_x\text{O}_4$ observed by SHG [27] and polarized neutron scattering [28] measurements. We argue that the physics in the hole-doped Sr_2IrO_4 is quite different than that on the electron-doped side. The Rh substitution [42–47] of the strongly SOC Ir in the Ir-O plane is very different than the electron doping by La substitution [48–50] in the off-plane charge reservoir layers or surface K doping [16,17,19,51]. Furthermore, a doped hole in Sr_2IrO_4 has a different electronic structure than that of an electron and is more likely to involve higher pseudospin states [52]. We therefore leave the hole-doped Sr_2IrO_4 aside and consider only the undoped and electron-doped Sr_2IrO_4 . Their unconventional low-energy quasiparticle properties observed by ARPES and STM have been described successfully by the hidden order of d PSCO [36] in the 2D limit of a single IrO_2 layer. Our focus in this paper is to investigate the effects of d PSCO on the symmetry properties of the 3D systems, which enables a

TABLE II. Symmetries of the coexistence states with possible c -axis stacking of CAF and d PSCO. The \checkmark/\times symbols mean the corresponding symmetry is preserved/broken in the coexistence state.

| Stacking | C_{2z} | M_z | I | T | C'_{2z} | M'_z | I' |
|---|--------------|--------------|--------------|--------------|--------------|--------------|--------------|
| + - - + / $\oplus \oplus \oplus \oplus$ | \times | \times | \checkmark | \times | \checkmark | \checkmark | \times |
| + - - + / $\oplus \oplus \oplus \oplus$ | \times | \checkmark | \times | \times | \checkmark | \times | \checkmark |
| + - - + / $\oplus \oplus \oplus \oplus$ | \checkmark | \checkmark | \checkmark | \checkmark | \checkmark | \checkmark | \checkmark |
| + - - + / $\oplus \oplus \oplus \oplus$ | \checkmark | \times | \times | \checkmark | \checkmark | \times | \times |
| + + - - / $\oplus \oplus \oplus \oplus$ | \times | \checkmark | \times | \times | \checkmark | \times | \checkmark |
| + + - - / $\oplus \oplus \oplus \oplus$ | \times | \times | \checkmark | \times | \checkmark | \checkmark | \times |
| + + - - / $\oplus \oplus \oplus \oplus$ | \checkmark | \checkmark | \checkmark | \checkmark | \checkmark | \checkmark | \checkmark |
| + + - - / $\oplus \oplus \oplus \oplus$ | \checkmark | \times | \times | \checkmark | \checkmark | \times | \times |
| + + + + / $\oplus \oplus \oplus \oplus$ | \times | \times | \checkmark | \times | \checkmark | \checkmark | \times |
| + + + + / $\oplus \oplus \oplus \oplus$ | \times | \times | \checkmark | \times | \checkmark | \checkmark | \times |
| + + + + / $\oplus \oplus \oplus \oplus$ | \times | \times | \checkmark | \times | \checkmark | \checkmark | \times |
| + + + + / $\oplus \oplus \oplus \oplus$ | \times | \times | \times | \checkmark | \checkmark | \times | \times |
| + - + - / $\oplus \oplus \oplus \oplus$ | \times | \checkmark | \times | \times | \checkmark | \times | \checkmark |
| + - + - / $\oplus \oplus \oplus \oplus$ | \times | \checkmark | \times | \times | \checkmark | \times | \checkmark |
| + - + - / $\oplus \oplus \oplus \oplus$ | \times | \checkmark | \times | \times | \checkmark | \times | \checkmark |
| + - + - / $\oplus \oplus \oplus \oplus$ | \times | \times | \times | \checkmark | \checkmark | \times | \times |

direct comparison with SHG and polarized neutron scattering experiments. At stoichiometry where these experiments have been conducted, the Néel temperature T_N and the hidden order transition temperature T_Q are very close to each other and barely distinguishable, thus providing us unambiguously only the symmetry information of the ground state, *i.e.*, the coexistence state of CAF and d PSCO.

The coexistence state has a symmetry only if there exists a lattice translation that simultaneously recovers both the CAF and the d PSCO states after the corresponding symmetry operation. Using the symmetries of the CAF and d PSCO summarized in Table I, the symmetries of the coexistence states are readily obtained, with the result given in Table II for all possible c -axis stacking patterns. Remarkably, there is one particular coexistence state, *i.e.*, + - - + / $\oplus \oplus \oplus \oplus$ with + - - + CAF and $\oplus \oplus \oplus \oplus$ d PSCO, whose magnetism and symmetry are compatible with current experimental observations for undoped Sr_2IrO_4 . Its magnetism is + - - + stacked CAF, and it breaks the twofold rotation, inversion, and time-reversal symmetries while preserving the mirror reflection symmetry. These properties make this coexistence state a promising candidate for the ground state of undoped Sr_2IrO_4 . Figure 2(a) shows the structure of the CAF and d PSCO in the + - - + / $\oplus \oplus \oplus \oplus$ coexistence state. The structure of d PSCO is illustrated by the symbols of \oplus and \ominus at the center of each Ir plaquette, which denote the direction of the associated pseudospin flux. The motion of the pseudospin-up and pseudospin-down electrons is not drawn here for the simplicity and visibility of the figure. The resultant structures, enclosed in the original unit cell, upon applying twofold rotation C_{2z} , mirror reflection M_z , inversion I , and time-reversal T are shown explicitly in Figs. 2(b)–2(e). It is clear that only the structure in Fig. 2(c) can recover the original structure in Fig. 2(a) after a lattice translation of $\tau_{yz} = (0, \frac{1}{2}, \frac{1}{2})$, while the other three structures could not recover that in Fig. 2(a) by any lattice translation.

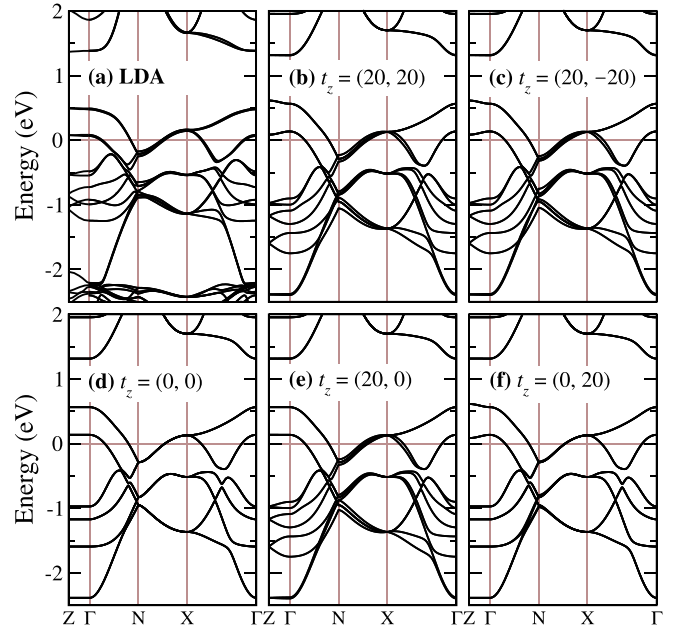


FIG. 3. Comparison of the band structures obtained using (a) local-density approximation (LDA) and (b)–(f) the three-dimensional five-orbital tight-binding (TB) + spin-orbit coupling (SOC) model with various interlayer hoppings $t_z = (t_{z1}, t_{z2})$ given in millielectronvolts. The high-symmetry points are labeled by $\Gamma = (0, 0, 0)$, $X = (\pi, 0, 0)$, $N = (\pi/2, \pi/2, 0)$, and $Z = (0, 0, \pi)$.

III. MICROSCOPIC MODELS

A. 3D TB + SOC model

The 2D TB + SOC model constructed in Ref. [36]:

$$\mathcal{H}_0 = \sum_{ij, \mu\nu, \sigma} t_{ij}^{\mu\nu, \sigma} d_{i\mu\sigma}^\dagger d_{j\nu\sigma} + \sum_{i\mu\sigma} \epsilon_{i\mu\sigma} d_{i\mu\sigma}^\dagger d_{i\mu\sigma} + \lambda_{\text{SOC}} \sum_{i, \mu\nu, \sigma\sigma'} \langle \mu | \mathbf{L} | \nu \rangle \cdot \langle \sigma | \mathbf{S} | \sigma' \rangle d_{i\mu\sigma}^\dagger d_{i\nu\sigma'}, \quad (1)$$

provides a faithful description of the density functional theory (DFT) band structure [Fig. 3(a)] downfolded to the five low-energy Ir $5d$ -electron orbitals, as shown in Fig. 3(d). Here, $d_{i\mu\sigma}^\dagger$ creates an electron with spin σ at site i in the μ th orbital defined in the local coordinate (X, Y, Z) that rotates with the IrO_6 octahedron, and $\mu = 1(d_{YZ}), 2(d_{ZX}), 3(d_{XY}), 4(d_{3Z^2-R^2}),$ and $5(d_{X^2-Y^2})$. The crystalline electric field effects are considered in the onsite energy term $\epsilon_{1, \dots, 5} = (0, 0, 202, 3054, 3831)$ meV, with a separation of $\Delta_c \equiv 10Dq \simeq 3.4$ eV between the t_{2g} and e_g complexes. The strength of atomic SOC $\lambda_{\text{SOC}} = 357$ meV. The spin and orbital angular momentum operators \mathbf{S} and \mathbf{L} have matrix elements $S_{\sigma\sigma'}^\eta = \langle \sigma | \mathbf{S} | \sigma' \rangle$ and $L_{\mu\nu}^\eta = \langle \mu | \mathbf{L} | \nu \rangle$, given explicitly in Ref. [36]. The spin- and orbital-dependent complex hopping integrals $t_{ij}^{\mu\nu, \sigma}$ between sites i and j in the realistic Sr_2IrO_4 with structural distortion are derived from those in the idealized Sr_2IrO_4 without structural distortion $\tilde{t}_{ij}^{\mu\nu, \sigma}$ by transforming the 10×10 hopping matrix $t_{ij} = \mathcal{R}_i^\dagger \tilde{t}_{ij} \mathcal{R}_j$. The operator $\mathcal{R}_i = e^{-iL_z \theta_i} \otimes e^{iS_z \theta_i}$ amounts to a joint spatial rotation from the global (x, y, z) to the local (X, Y, Z) coordinates by θ_i and a spin rotation by the same angle θ_i . Note that there is a 45° rotation between the x, y axis of the global

coordinate defined in this section and the a, b axis used in Sec. II, as shown in the inset in Fig. 1. In the undistorted idealized systems, the hopping integrals $\tilde{t}_{ij}^{\mu\nu,\sigma}$ are real, spin independent, and given in Ref. [36] explicitly up to the fifth nearest neighbors in a IrO_2 layer.

To construct a realistic 3D model for Sr_2IrO_4 , in addition to the in-plane \tilde{t}_{ij} given in Ref. [36], we include nonzero \tilde{t}_{ij} on the nearest neighbor (NN) interlayer bonds, *i.e.*, site i and j from two adjacent IrO_2 layers. Owing to the shift between adjacent IrO_2 ab planes, as shown in Fig. 2(a), there are eight interlayer NN sites for each Ir atom, four in the layer right above it and the other four in the layer right below it. The inter-layer hoppings can be limited to the t_{2g} orbitals since the contribution from the e_g orbitals to the low-energy states is negligible small. Furthermore, the interlayer hoppings involving the planar orbital d_{xy} are expected to be small. In fact, any significant interlayer intraorbital hopping of the d_{xy} orbital would split the bands ~ -2 eV below the Fermi level, clearly incompatible with the LDA band structures shown in Fig. 3(a). We thus consider only interlayer hoppings involving the d_{yz} and d_{zx} orbitals $t_z = (t_{z1}, t_{z2})$, where t_{z1} and t_{z2} denotes, respectively, the intraorbital and interorbital hoppings. While the intraorbital hoppings are isotropic on the interlayer NN bonds, the interorbital hoppings are anisotropic, taking values $\pm t_{z2}$ on the four interlayer NN bonds parallel to the $[1, \pm 1, 0]$ plane in the (x, y, z) global coordinates.

Figures 3(b)–3(f) show the electronic structures of the 3D TB + SOC model with various interlayer hoppings $t_z = (t_{z1}, t_{z2})$ in comparison with the local-density approximation (LDA) band structure plotted in Fig. 3(a). Note that the band structures for opposite interlayer hoppings (*i.e.*, $t_z \rightarrow -t_z$) are identical and remain equivalent even in the presence of Hubbard interaction and d PSCO considered in the following subsections. We therefore fix the intraorbital t_{z1} to be positive. Figure 3(d) displays the band structure of the 2D TB + SOC model without any interlayer hopping $t_z = 0$, and Figs. 3(e) and 3(f) show, respectively, the individual effects of the intraorbital t_{z1} and interorbital t_{z2} on the band structure. Clearly, t_{z2} does little to the band structure, while t_{z1} splits the bands and thus captures the essential inter-layer features of the LDA bands displayed in Fig. 3(a). The splitting is $\sim 4t_{z1}$ at the N point for the bands right below the Fermi level. Therefore, an intraorbital t_{z1} of 20 meV would reproduce the ~ 78 meV band splitting in the LDA bands. The effects of the interorbital t_{z2} on the band structures are negligible even in the presence of nonzero t_{z1} , as shown in Figs. 3(b) and 3(c). Consequently, t_{z2} remains a tunable band parameter that shall be determined later by the c -axis stacking of the magnetism.

B. Stacking of CAF

To investigate the magnetism in Sr_2IrO_4 , we consider the 3D five-orbital Hubbard model $\mathcal{H} = \mathcal{H}_0 + \mathcal{H}_U$, with the electron correlations described by the standard multiorbital Hubbard interactions:

$$\begin{aligned} \mathcal{H}_U = & U \sum_{i,\mu} \hat{n}_{i\mu\uparrow} \hat{n}_{i\mu\downarrow} + \left(U' - \frac{J_H}{2} \right) \sum_{i,\mu < \nu} \hat{n}_{i\mu} \hat{n}_{i\nu} \\ & - J_H \sum_{i,\mu \neq \nu} \mathbf{S}_{i\mu} \cdot \mathbf{S}_{i\nu} + J_H \sum_{i,\mu \neq \nu} d_{i\mu\uparrow}^\dagger d_{i\mu\downarrow}^\dagger d_{i\nu\downarrow} d_{i\nu\uparrow}, \quad (2) \end{aligned}$$

where U and U' are the local intraorbital and interorbital Coulomb repulsions and J_H is the Hund's rule coupling with the relation of $U = U' + 2J_H$. Note that, in Eq. (2), for the complete set of five d orbitals, J_H should be understood as an average of the exchange interactions of the t_{2g} and e_g orbitals since the difference between them is usually small in cubic systems [53,54]. The interactions in Eq. (2) are treated within the Hartree-Fock approximations. In the presence of SOC, the Hartree and exchange self-energies induced by \mathcal{H}_U depend on the full spin-orbital-dependent density matrix $n_{i\sigma\sigma'}^{\mu\nu} = \langle d_{i\mu\sigma}^\dagger d_{i\nu\sigma'} \rangle$, which are determined self-consistently in the numerical calculations. Local physical quantities in the ground state can be expressed in terms of $n_{i\sigma\sigma'}^{\mu\nu}$, the local spin density $S_i^\eta = \sum_{\mu,\sigma\sigma'} S_{\sigma\sigma'}^\eta n_{i\sigma\sigma'}^{\mu\mu}$, and the local orbital angular momentum $L_i^\eta = \sum_{\mu \neq \nu, \sigma} n_{i\sigma\sigma}^{\mu\nu} L_{\mu\nu}^\eta$. In all calculations presented in this paper, we choose $(U, J_H) = (1.2, 0.05)$ eV that, in the 2D calculations [36], correctly produces the CAF as the magnetic ground state for the undoped Sr_2IrO_4 and the low-energy quasiparticle properties in good agreement with ARPES measurements [15].

We first verify numerically the one-to-one correspondence, discussed in the previous section, between the CAF states with a FM moment along the a axis and those with a FM moment along the b axis. The direction of the net FM moment can be pinned by choosing appropriate initial values for $n_{i\sigma\sigma'}^{\mu\nu}$. In numerical calculations, an octant of the reduced Brillouin zone, corresponding to the conventional unit cell with eight Ir atoms shown in Fig. 2(a), is discretized evenly into $L_x \times L_y \times L_z$ \mathbf{k} -points. We obtain these states self-consistently at various $L_x \times L_y \times L_z$ and compare their energies. Figure 4(a) plots the energy difference between the $(+ - +)_a$ and $(+ + -)_b$ CAF states as a function of the in-plane \mathbf{k} -point $L_x \times L_y$, with the interlayer hopping fixed to be $t_z = (20, -20)$ meV. The energy difference is not sensitive to L_z , probably because the interlayer hoppings t_z are much smaller in amplitude than the in-plane hoppings. Except for the first two data points, the energy difference is < 0.01 μeV per site, within the resolution of our numerical calculations. We thus conclude that the $(+ - +)_a$ and $(+ + -)_b$ CAF states are equivalent, consistent with the symmetry analysis. The correspondences between other states are also verified numerically. To reduce the finite-sized effect, we take $L_x \times L_y \times L_z = 601 \times 600 \times 10$ in the rest of the paper.

In the absence of interorbital hopping $t_{z2} = 0$, the intraorbital t_{z1} dependence of the state energy of $+ - +$, $+ + -$, and $+ + +$ CAFs is shown in Fig. 4(b) with respect to that of the $+ - +$ CAF. Clearly, the $+ - +$ and $+ + -$ CAFs are identical in energy at any intraorbital t_{z1} , implying the absence of the in-plane anisotropy. It is thus equivalent for the net FM moment to align in either the a axis or in the b axis, in the absence of t_{z2} . The intraorbital t_{z1} energetically favors the $+ - +$ CAF, while it disfavors mostly the $+ + +$ CAF. Fixing intraorbital $t_{z1} = 20$ meV by the ~ 78 meV band splitting in LDA, Fig. 4(c) plots the energies of the CAF states as a function of interorbital t_{z2} . While the $+ - +$ CAF is the most disfavored magnetic state on the positive t_{z2} side, there is a wide range on the negative side $t_{z2} \in (-38, -6)$ meV, where the $+ - +$ CAF becomes the lowest in energy, supporting the ground magnetic structure revealed in experiments [2,26]. Furthermore, the $+ + +$ CAF is higher in energy by

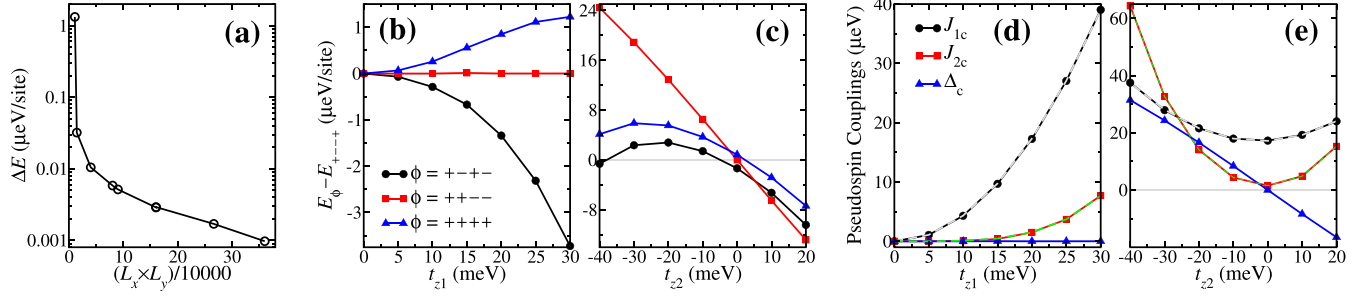


FIG. 4. (a) Energy difference between $(+-+)_a$ and $(++-)_b$ canted antiferromagnet (CAF) as a function of $L_x \times L_y$, the number of in-plane \mathbf{k} -points. The total number of \mathbf{k} -points $L_x \times L_y \times L_z$ in an octant of the three-dimensional reduced Brillouin zone is, for the nine data points from left to right, $121 \times 90 \times 20$, $121 \times 120 \times 110$, $201 \times 200 \times 40$, $284 \times 283 \times 20$, $301 \times 300 \times 60$, $401 \times 400 \times 10$, $401 \times 400 \times 80$, $517 \times 516 \times 6$, and $601 \times 600 \times 10$. The interlayer hopping $t_z = (20, -20)$ meV. (b) Intraorbital t_{z1} dependence of the CAF state energies in the absence of interorbital hopping $t_{z2} = 0$. (c) Interorbital t_{z2} dependence of the CAF state energies with intraorbital $t_{z1} = 20$ meV. Data in (b) and (c) are obtained with $L_x \times L_y \times L_z = 601 \times 600 \times 10$. (d) Intraorbital t_{z1} dependence of the interlayer pseudospin couplings with $t_{z2} = 0$. (e) Interorbital t_{z2} dependence of the interlayer pseudospin couplings with $t_{z1} = 20$ meV. Gray/green dashed lines in (d) and (e) are fits to the data by quadratic/quartic functions.

$\sim 5 \mu\text{eV}$ per site at $t_{z2} = -20$ meV, which agrees remarkably well with the ~ 0.3 T external magnetic field required in experiments to align all FM moments along one direction [2].

Within the pseudospin-only models [39,55], it has been shown that the c -axis stacking of the static long-range magnetic order in the undoped Sr_2IrO_4 is stabilized by the interplay of interlayer pseudospin couplings, including the first-nearest-interlayer interaction J_{1c} , the second-nearest-interlayer interaction J_{2c} , and the anisotropy Δ_c , which comes from the anisotropic interlayer interaction [56]. In terms of the effective couplings between the net moments ($\tilde{\mathbf{S}} = \mathbf{L} + 2\mathbf{S}$), $j_{1c} = 4J_{1c}\tilde{S}^2 \sin^2 \theta$, $j_{2c} = -J_{2c}\tilde{S}^2(\cos^2 \theta - \sin^2 \theta)$, and $\delta_c = 4\Delta_c\tilde{S}^2 \cos^2 \theta$, the energies of the $+-+$, $++-$, $+ - + -$, and $++++$ CAF states are, respectively, $-\delta_c - j_{2c}$, $\delta_c - j_{2c}$, $-j_{1c} + j_{2c}$, and $j_{1c} + j_{2c}$. In the CAF states obtained self-consistently at Hubbard interactions $(U, J) = (1.2, 0.05)$ eV, the ordered pseudospin moment $\tilde{S} \simeq 0.67 \mu_B$, and the canting angle $\theta \simeq 22^\circ$. It is readily and instructive to extract, from the Hartree-Fock state energies given in Figs. 4(b) and 4(c), the values of J_{1c} , J_{2c} , and Δ_c . The interlayer pseudospin couplings are plotted in Fig. 4(d) as a function of intraorbital t_{z1} in the absence of interorbital $t_{z2} = 0$ and in Fig. 4(e) as a function of interorbital t_{z2} with the intraorbital hopping fixed to be $t_{z1} = 20$ meV. Clearly, the intraorbital t_{z1} does not generate any anisotropy Δ_c , while the interorbital t_{z2} produces an anisotropy linear in t_{z2} . In the absence of t_{z2} , the intraorbital t_{z1} produces a $J_{1c} \propto t_{z1}^2$ and a $J_{2c} \propto t_{z1}^4$, as shown in Fig. 4(d). At a fixed nonzero intraorbital t_{z1} , the superexchange interactions J_{1c} and J_{2c} generated by interorbital t_{z2} can be well fitted by quadratic and quartic functions of t_{z2} , respectively, as shown in Fig. 4(e). These behaviors are consistent with the fact that superexchange interactions J_{1c} and J_{2c} are generated by, respectively, the second- and quadratic-order perturbations in the interlayer hoppings. Interestingly, at $t_z = (20, -20)$ meV, the interlayer pseudospin couplings $(J_{1c}, J_{2c}, \Delta_c) = (21.6, 14.0, 16.6) \mu\text{eV}$ are consistent with the values extracted from experiment [39].

Figure 5 displays the band dispersions of the CAF states with different c -axis stackings. They are all AFM insulators

with a similar overall structure. The quasiparticle band below the AFM gap has an eightfold degeneracy at the X point, four of them due to the folding along the c axis of the conventional unit cell and the other two are protected by the twofold rotation symmetry C_{2a} about the a axis, along which the FM moment aligned. These eight bands behave differently along the X - N direction, which is probably the most pronounced difference among these band structures. They remain degenerate in the $+-+$ CAF, split into three branches in the $++-$ CAF, but split into two branches in the $+ - + -$ and $++++$ CAF states.

C. Stacking of $d\text{PSCO}$

The physical origin of the $d\text{PSCO}$ is still under investigation [36] and out of the scope of this paper. Therefore, unlike the CAF, its stacking pattern could not be determined self-consistently by including in the Hamiltonian an interaction term from which the $d\text{PSCO}$ develops spontaneously. Instead, we determine its c -axis stacking via a variational approach. Explicitly, a variational term for the $d\text{PSCO}$, \mathcal{H}_Δ , is added to the Hamiltonian $\mathcal{H} = \mathcal{H}_0 + \mathcal{H}_U + \mathcal{H}_\Delta$, with

$$\mathcal{H}_\Delta = i\Delta \sum_{i \in A, \sigma} \sum_{j=i+\delta} \eta_i \tau_{ij} \sigma (\gamma_{i\sigma}^\dagger \gamma_{j\sigma} - \chi_{ij}^\sigma) + \text{H.c.}, \quad (3)$$

where the NN vector $\delta = \{\pm\hat{x}, \pm\hat{y}\}$, the standard NN d -wave form factor $\tau_{ij} = (-1)^{i_x + j_y}$, and $\chi_{ij}^\sigma = \langle \gamma_{i\sigma}^\dagger \gamma_{j\sigma} \rangle$, whose presence ensures that the variational term \mathcal{H}_Δ does not add an elastic part to the state energy. The operator $\gamma_\sigma = \frac{1}{\sqrt{3}}(i\sigma d_{yz, \bar{\sigma}} + d_{zx, \bar{\sigma}} + id_{xy, \sigma})$ annihilates the $J_{\text{eff}} = \frac{1}{2}$ doublet in the quasiparticle excitations, $|J = \frac{1}{2}, J_z = \pm \frac{1}{2}\rangle = \gamma_\pm^\dagger |0\rangle$. The c -axis stacking of $d\text{PSCO}$ is then controlled by η_i as it takes on values of ± 1 for the Ir site i in different IrO_2 layers. For example, to generate the $\oplus \oplus \ominus \ominus$ stacking pattern for $d\text{PSCO}$, η_i take the values of $+1, +1, -1, -1$, respectively, for lattice site i in the four IrO_2 layers. We fix the stacking pattern of CAF to be $+-+$ and try to find the energetically preferred stacking pattern of $d\text{PSCO}$ in the coexistence state.

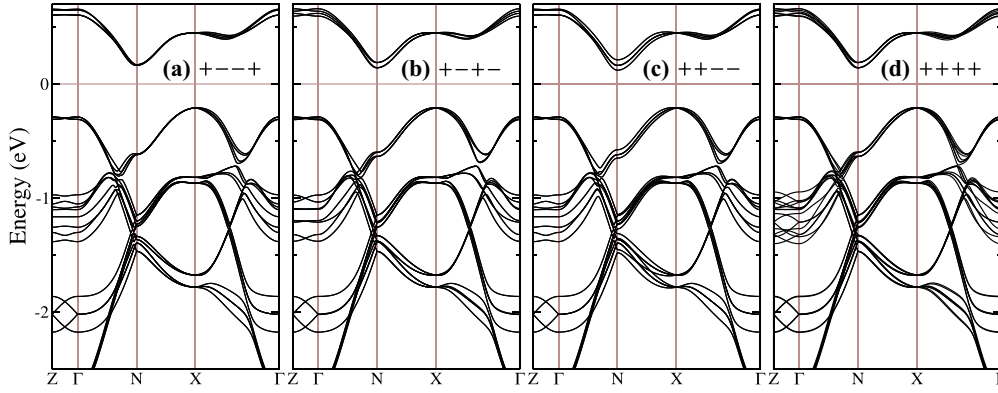


FIG. 5. Comparison between the band dispersions of the canted antiferromagnet (CAF) states with various c -axis stacking. The interlayer hoppings $t_z = (20, -20)$ meV, and the Hubbard interactions $(U, J) = (1.2, 0.05)$ eV.

The interlayer hoppings are chosen to be $t_z = (20, -20)$ meV, where the $+ - - +$ CAF is the magnetic ground state. At a given strength of d PSCO, Δ , we obtain the coexistence states of $+ - - +$ CAF with four possible c -axis stacked d PSCO self-consistently and then compare their energies to find the preferred stacking pattern for the d PSCO. The energies of the coexistence states with $\oplus \oplus \oplus \oplus$, $\oplus \oplus \oplus \ominus$, and $\oplus \oplus \ominus \ominus$ d PSCO are plotted in Fig. 6(a) as a function of Δ , with respect to that of the coexistence state with $\oplus \oplus \ominus \ominus$ d PSCO. It is clear that the $+ - - + / \oplus \oplus \ominus \ominus$ coexistence state is energetically favored over all other coexistence states, and as shown in Sec. II, its symmetry is compatible with available experimental observations on undoped Sr_2IrO_4 below the Néel temperature T_N .

The band dispersions of the four coexistence states with $+ - - +$ CAF are plotted in Figs. 6(b)–6(e) for $\Delta = 30$ meV. The d PSCO order breaks the C_{2a} symmetry, splits the eightfold degenerate band at the X point into two fourfold degenerate branches, giving rise to a band splitting of ~ 200 meV at the X point. We note that the C_{2a} symmetry is broken by the staggered tetragonal distortion of the IrO_6 octahedra at temperatures above T_Ω in undoped Sr_2IrO_4 [23–26]. However, the tetragonal distortion would split the degenerate bands evenly by a constant along N - X ; thus unable to capture the unconventional quasiparticle properties of Sr_2IrO_4 in both the

undoped magnetic insulating phase and the electron-doped nonmagnetic phase.

IV. DISCUSSIONS AND SUMMARIES

The existence and the nature of a hidden order in Sr_2IrO_4 have been under intensive debate. After the observation of the anomalous SHG signal [27], polarized neutron diffraction [28] and muon spin relaxation [29] measurements performed on undoped and hole-doped Sr_2IrO_4 revealed broken time-reversal symmetry below T_Ω . Furthermore, magnetic resonant x-ray scattering measurements [50] conducted on the electron-doped Sr_2IrO_4 have uncovered a unidirectional spin density wave state in the pseudogap phase. These experimental observations support the idea that the pseudogap is associated with a symmetry-breaking hidden order. On the other hand, alternative explanations without invoking loop currents were proposed for the anomalous SHG signal, including laser-induced rearrangement of the magnetic stacking and enhanced sensitivity to surface rather than bulk magnetism [41]. More recent comprehensive experiments [35] conducted on undoped Sr_2IrO_4 have ruled out the possibility of laser-induced rearrangement of the magnetic stacking and suggest that the surface-magnetization-induced electric-dipole process in the SHG experiments can be strongly enhanced by

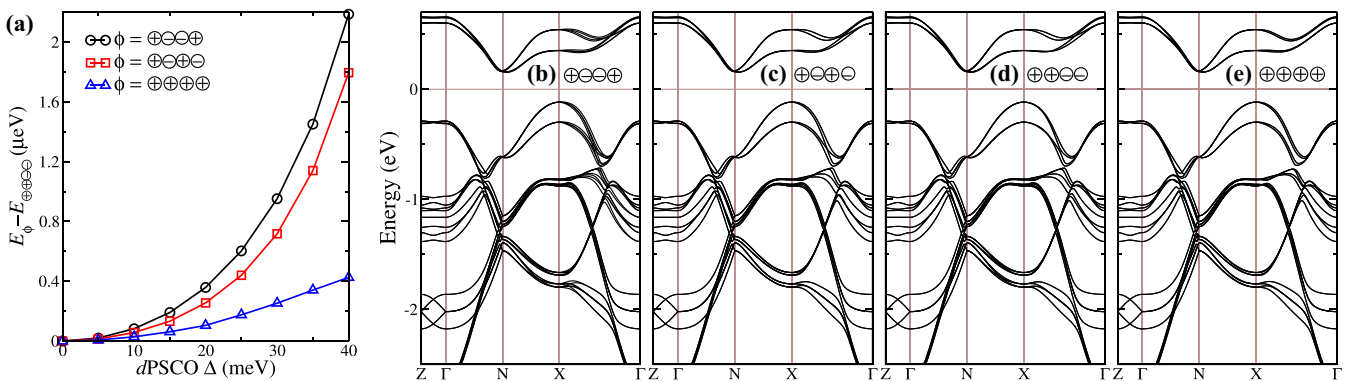


FIG. 6. (a) The state energies of the coexistence states as a function of the d -wave pseudospin current order (d PSCO) order Δ . The stacking pattern of the canted antiferromagnet (AFM) is fixed to be $+ - - +$, and the interlayer hopping $t_z = (20, -20)$ meV. (b)–(e) Comparison of the band dispersions of the coexistence states with various c -axis stacking of d PSCO ($\Delta = 30$ meV).

SOC. However, the existence of a hidden order in Sr_2IrO_4 remains a possible explanation for the experimental observations of symmetry breaking and unconventional quasiparticle excitations.

In this paper, we have shown that the coexistence state of $+ - - +$ CAF and $\oplus \oplus \ominus \ominus$ d PSCO has all the symmetry properties compatible with the available experimental observations on the undoped Sr_2IrO_4 below the Néel temperature T_N . It is a magnetoelectric state that breaks the twofold rotation C_{2z} , inversion I , and time-reversal T symmetries. We then demonstrated its microscopic realization in a realistic 3D Hubbard model with SOC and structural distortion. Together with the fact that the highly unconventional quasiparticle properties observed in both the parent and electron-doped Sr_2IrO_4 can be described remarkably well by the d PSCO [36], the latter offers a promising candidate for the hidden order responsible for the pseudogap phase in the undoped and electron-doped iridates. Since the Néel temperature T_N and the hidden order transition temperature T_Ω are very close to each other in undoped Sr_2IrO_4 , available experiments could not tell us unambiguously the symmetry properties of the

pseudogap phase. It is thus very desirable to carry out optical SHG and neutron scattering experiments on the pseudogap phase in electron-doped Sr_2IrO_4 . In the absence of magnetism, the d PSCO would preserve the spatial inversion and time-reversal symmetries but lower the fourfold rotation symmetry to twofold C_{2z} due to the d -wave form factor. It would be interesting to calculate the magnetic excitations in the non-magnetic d PSCO state and make a comparison with magnetic resonant x-ray scattering observations [50].

ACKNOWLEDGMENTS

Y.-P.H., J.-W.D., and S.Z. are supported by the Strategic Priority Research Program of CAS (Grant No. XDB28000000) and the National Natural Science Foundation of China (Grants No. 11974362 and No. 12047503). Z.W. is supported by the U.S. Department of Energy, Basic Energy Sciences (Grant No. DE-FG02-99ER45747). Numerical calculations in this paper were performed on the High-Performance Computing (HPC) Cluster of ITP-CAS.

-
- [1] B. J. Kim, H. Jin, S. J. Moon, J.-Y. Kim, B.-G. Park, C. S. Leem, J. Yu, T. W. Noh, C. Kim, S.-J. Oh *et al.*, Novel $J_{\text{eff}} = \frac{1}{2}$ Mott State Induced by Relativistic Spin-Orbit Coupling in Sr_2IrO_4 , *Phys. Rev. Lett.* **101**, 076402 (2008).
- [2] B. J. Kim, H. Ohsumi, T. Komesu, S. Sakai, T. Morita, H. Takagi, and T. Arima, Phase-Sensitive Observation of a Spin-Orbital Mott State in Sr_2IrO_4 , *Science* **323**, 1329 (2009).
- [3] D. Pesin and L. Balents, Mott physics and band topology in materials with strong spin-orbit interaction, *Nat. Phys.* **6**, 376 (2010).
- [4] W. Witczak-Krempa, G. Chen, Y. B. Kim, and L. Balents, Correlated quantum phenomena in the strong spin-orbit regime, *Annu. Rev. Condens. Matter Phys.* **5**, 57 (2014).
- [5] J. G. Rau, E. K.-H. Lee, and H.-Y. Kee, Spin-orbit physics giving rise to novel phases in correlated systems: Iridates and related materials, *Annu. Rev. Condens. Matter Phys.* **7**, 195 (2016).
- [6] R. Schaffer, E. K.-H. Lee, B.-J. Yang, and Y. B. Kim, Recent progress on correlated electron systems with strong spin-orbit coupling, *Rep. Prog. Phys.* **79**, 094504 (2016).
- [7] S. M. Winter, A. A. Tsirlin, M. Daghofer, J. van den Brink, Y. Singh, P. Gegenwart, and R. Valenti, Models and materials for generalized Kitaev magnetism, *J. Phys.: Condens. Matter* **29**, 493002 (2017).
- [8] M. Hermanns, I. Kimchi, and J. Knolle, Physics of the Kitaev model: Fractionalization, dynamic correlations, and material connections, *Annu. Rev. Condens. Matter Phys.* **9**, 17 (2018).
- [9] J. Dai, E. Calleja, G. Cao, and K. McElroy, Local density of states study of a spin-orbit-coupling induced Mott insulator Sr_2IrO_4 , *Phys. Rev. B* **90**, 041102(R) (2014).
- [10] J. Kim, D. Casa, M. H. Upton, T. Gog, Y.-J. Kim, J. F. Mitchell, M. van Veenendaal, M. Daghofer, J. van den Brink, G. Khaliullin *et al.*, Magnetic Excitation Spectra of Sr_2IrO_4 Probed by Resonant Inelastic X-Ray Scattering: Establishing Links to Cuprate Superconductors, *Phys. Rev. Lett.* **108**, 177003 (2012).
- [11] F. Wang and T. Senthil, Twisted Hubbard Model for Sr_2IrO_4 : Magnetism and Possible High Temperature Superconductivity, *Phys. Rev. Lett.* **106**, 136402 (2011).
- [12] Y. Yang, W.-S. Wang, J.-G. Liu, H. Chen, J.-H. Dai, and Q.-H. Wang, Superconductivity in doped Sr_2IrO_4 : A functional renormalization group study, *Phys. Rev. B* **89**, 094518 (2014).
- [13] H. Watanabe, T. Shirakawa, and S. Yunoki, Monte Carlo Study of an Unconventional Superconducting Phase in Iridium Oxide $J_{\text{eff}} = \frac{1}{2}$ Mott Insulators Induced by Carrier Doping, *Phys. Rev. Lett.* **110**, 027002 (2013).
- [14] Z. Y. Meng, Y. B. Kim, and H.-Y. Kee, Odd-Parity Triplet Superconducting Phase in Multiorbital Materials with a Strong Spin-Orbit Coupling: Application to Doped Sr_2IrO_4 , *Phys. Rev. Lett.* **113**, 177003 (2014).
- [15] A. de la Torre, S. McKeown Walker, F. Y. Bruno, S. Ricco, Z. Wang, I. Gutierrez Lezama, G. Scheerer, G. Giriat, D. Jaccard, C. Berthod *et al.*, Collapse of the Mott Gap and Emergence of a Nodal Liquid in Lightly Doped Sr_2IrO_4 , *Phys. Rev. Lett.* **115**, 176402 (2015).
- [16] Y. K. Kim, O. Krupin, J. D. Denlinger, A. Bostwick, E. Rotenberg, Q. Zhao, J. F. Mitchell, J. W. Allen, and B. J. Kim, Fermi arcs in a doped pseudospin- $\frac{1}{2}$ Heisenberg antiferromagnet, *Science* **345**, 187 (2014).
- [17] Y. J. Yan, M. Q. Ren, H. C. Xu, B. P. Xie, R. Tao, H. Y. Choi, N. Lee, Y. J. Choi, T. Zhang, and D. L. Feng, Electron-Doped Sr_2IrO_4 : An Analogue of Hole-Doped Cuprate Superconductors Demonstrated by Scanning Tunneling Microscopy, *Phys. Rev. X* **5**, 041018 (2015).
- [18] I. Battisti, K. M. Bastiaans, V. Fedoseev, A. De La Torre, N. Iliopoulos, A. Tamai, E. C. Hunter, R. S. Perry, J. Zaanen, F. Baumberger *et al.*, Universality of pseudogap and emergent order in lightly doped Mott insulators, *Nat. Phys.* **13**, 21 (2017).

- [19] Y. K. Kim, N. Sung, J. Denlinger, and B. Kim, Observation of a d -wave gap in electron-doped Sr_2IrO_4 , *Nat. Phys.* **12**, 37 (2016).
- [20] H. Zhao, S. Manna, Z. Porter, X. Chen, A. Uzdeczyk, J. Moodera, Z. Wang, S. D. Wilson, and I. Zeljkovic, Atomic-scale fragmentation and collapse of antiferromagnetic order in a doped Mott insulator, *Nat. Phys.* **15**, 1267 (2019).
- [21] S. Boseggia, H. C. Walker, J. Vale, R. Springell, Z. Feng, R. S. Perry, M. M. Sala, H. M. Rønnow, S. P. Collins, and D. F. McMorrow, Locking of iridium magnetic moments to the correlated rotation of oxygen octahedra in Sr_2IrO_4 revealed by x-ray resonant scattering, *J. Phys.: Condens. Matter* **25**, 422202 (2013).
- [22] M. K. Crawford, M. A. Subramanian, R. L. Harlow, J. A. Fernandez-Baca, Z. R. Wang, and D. C. Johnston, Structural and magnetic studies of Sr_2IrO_4 , *Phys. Rev. B* **49**, 9198 (1994).
- [23] F. Ye, S. Chi, B. C. Chakoumakos, J. A. Fernandez-Baca, T. Qi, and G. Cao, Magnetic and crystal structures of Sr_2IrO_4 : A neutron diffraction study, *Phys. Rev. B* **87**, 140406(R) (2013).
- [24] C. Dhital, T. Hogan, Z. Yamani, C. de la Cruz, X. Chen, S. Khadka, Z. Ren, and S. D. Wilson, Neutron scattering study of correlated phase behavior in Sr_2IrO_4 , *Phys. Rev. B* **87**, 144405 (2013).
- [25] D. H. Torchinsky, H. Chu, L. Zhao, N. B. Perkins, Y. Sizyuk, T. Qi, G. Cao, and D. Hsieh, Structural Distortion-Induced Magnetoelastic Locking in Sr_2IrO_4 Revealed through Nonlinear Optical Harmonic Generation, *Phys. Rev. Lett.* **114**, 096404 (2015).
- [26] S. Boseggia, R. Springell, H. C. Walker, H. M. Rønnow, C. Rüegg, H. Okabe, M. Isobe, R. S. Perry, S. P. Collins, and D. F. McMorrow, Robustness of Basal-Plane Antiferromagnetic Order and the $J_{\text{eff}} = \frac{1}{2}$ State in Single-Layer Iridate Spin-Orbit Mott Insulators, *Phys. Rev. Lett.* **110**, 117207 (2013).
- [27] L. Zhao, D. Torchinsky, H. Chu, V. Ivanov, R. Lifshitz, R. Flint, T. Qi, G. Cao, and D. Hsieh, Evidence of an odd-parity hidden order in a spin-orbit coupled correlated iridate, *Nat. Phys.* **12**, 32 (2016).
- [28] J. Jeong, Y. Sidis, A. Louat, V. Brouet, and P. Bourges, Time-reversal symmetry breaking hidden order in $\text{Sr}_2(\text{Ir}, \text{Rh})\text{O}_4$, *Nat. Commun.* **8**, 15119 (2017).
- [29] C. Tan, Z. F. Ding, J. Zhang, Z. H. Zhu, O. O. Bernal, P. C. Ho, A. D. Hillier, A. Koda, H. Luetkens, G. D. Morris *et al.*, Slow magnetic fluctuations and critical slowing down in $\text{Sr}_2\text{Ir}_{1-x}\text{Rh}_x\text{O}_4$, *Phys. Rev. B* **101**, 195108 (2020).
- [30] H. Murayama, K. Ishida, R. Kurihara, T. Ono, Y. Sato, Y. Kasahara, H. Watanabe, Y. Yanase, G. Cao, Y. Mizukami *et al.*, Bond Directional Anapole Order in a Spin-Orbit Coupled Mott Insulator $\text{Sr}_2(\text{Ir}_{1-x}\text{Rh}_x)\text{O}_4$, *Phys. Rev. X* **11**, 011021 (2021).
- [31] C. M. Varma, Non-Fermi-liquid states and pairing instability of a general model of copper oxide metals, *Phys. Rev. B* **55**, 14554 (1997).
- [32] C. M. Varma, Theory of the pseudogap state of the cuprates, *Phys. Rev. B* **73**, 155113 (2006).
- [33] C. M. Varma, Pseudogap in cuprates in the loop-current ordered state, *J. Phys.: Condens. Matter* **26**, 505701 (2014).
- [34] S. J. Moon, M. W. Kim, K. W. Kim, Y. S. Lee, J.-Y. Kim, J.-H. Park, B. J. Kim, S.-J. Oh, S. Nakatsuji, Y. Maeno *et al.*, Electronic structures of layered perovskite Sr_2MO_4 ($M = \text{Ru}, \text{Rh}, \text{and Ir}$), *Phys. Rev. B* **74**, 113104 (2006).
- [35] K. L. Seyler, A. de la Torre, Z. Porter, E. Zoghlin, R. Polshi, M. Nguyen, S. Nadj-Perge, S. D. Wilson, and D. Hsieh, Spin-orbit-enhanced magnetic surface second-harmonic generation in Sr_2IrO_4 , *Phys. Rev. B* **102**, 201113(R) (2020).
- [36] S. Zhou, K. Jiang, H. Chen, and Z. Wang, Correlation Effects and Hidden Spin-Orbit Entangled Electronic Order in Parent and Electron-Doped Iridates Sr_2IrO_4 , *Phys. Rev. X* **7**, 041018 (2017).
- [37] J. W. Han, S.-W. Kim, W. S. Kyung, C. Kim, G. Cao, X. Chen, S. D. Wilson, S. Cheon, and J. S. Lee, Nonsymmorphic Dirac semimetal and carrier dynamics in the doped spin-orbit-coupled Mott insulator Sr_2IrO_4 , *Phys. Rev. B* **102**, 041108(R) (2020).
- [38] S.-W. Kim, M. Kang, and S. Cheon, Low-energy electrodynamic of Dirac semimetal phases in the doped Mott insulator Sr_2IrO_4 , *Phys. Rev. B* **103**, 045116 (2021).
- [39] J. Porras, J. Bertinshaw, H. Liu, G. Khaliullin, N. H. Sung, J.-W. Kim, S. Francoual, P. Steffens, G. Deng, M. M. Sala *et al.*, Pseudospin-lattice coupling in the spin-orbit Mott insulator Sr_2IrO_4 , *Phys. Rev. B* **99**, 085125 (2019).
- [40] H. Liu and G. Khaliullin, Pseudo-Jahn-Teller Effect and Magnetoelastic Coupling in Spin-Orbit Mott Insulators, *Phys. Rev. Lett.* **122**, 057203 (2019).
- [41] S. Di Matteo and M. R. Norman, Magnetic ground state of Sr_2IrO_4 and implications for second-harmonic generation, *Phys. Rev. B* **94**, 075148 (2016).
- [42] T. F. Qi, O. B. Korneta, L. Li, K. Butrouna, V. S. Cao, X. Wan, P. Schlottmann, R. K. Kaul, and G. Cao, Spin-orbit tuned metal-insulator transitions in single-crystal $\text{Sr}_2\text{Ir}_{1-x}\text{Rh}_x\text{O}_4$ ($0 \leq x \leq 1$), *Phys. Rev. B* **86**, 125105 (2012).
- [43] J. P. Clancy, A. Lupascu, H. Gretarsson, Z. Islam, Y. F. Hu, D. Casa, C. S. Nelson, S. C. LaMarra, G. Cao, and Y.-J. Kim, Dilute magnetism and spin-orbital percolation effects in $\text{Sr}_2\text{Ir}_{1-x}\text{Rh}_x\text{O}_4$, *Phys. Rev. B* **89**, 054409 (2014).
- [44] F. Ye, X. Wang, C. Hoffmann, J. Wang, S. Chi, M. Matsuda, B. C. Chakoumakos, J. A. Fernandez-Baca, and G. Cao, Structure symmetry determination and magnetic evolution in $\text{Sr}_2\text{Ir}_{1-x}\text{Rh}_x\text{O}_4$, *Phys. Rev. B* **92**, 201112(R) (2015).
- [45] Y. Cao, Q. Wang, J. A. Waugh, T. J. Reber, H. Li, X. Zhou, S. Parham, S.-R. Park, N. C. Plumb, E. Rotenberg *et al.*, Hallmarks of the Mott-metal crossover in the hole-doped pseudospin- $\frac{1}{2}$ Mott insulator Sr_2IrO_4 , *Nat. Commun.* **7**, 11367 (2016).
- [46] V. Brouet, J. Mansart, L. Perfetti, C. Piovera, I. Vobornik, P. Le Fèvre, F. Bertran, S. C. Riggs, M. C. Shapiro, P. Giraldo-Gallo *et al.*, Transfer of spectral weight across the gap of Sr_2IrO_4 induced by La doping, *Phys. Rev. B* **92**, 081117(R) (2015).
- [47] S. Chikara, G. Fabbris, J. Terzic, G. Cao, D. Khomskii, and D. Haskel, Charge partitioning and anomalous hole doping in Rh-doped Sr_2IrO_4 , *Phys. Rev. B* **95**, 060407(R) (2017).
- [48] H. Gretarsson, N. H. Sung, J. Porras, J. Bertinshaw, C. Dietl, J. A. N. Bruin, A. F. Bangura, Y. K. Kim, R. Dinnebieer, J. Kim *et al.*, Persistent Paramagnons Deep in the Metallic Phase of $\text{Sr}_{2-x}\text{La}_x\text{IrO}_4$, *Phys. Rev. Lett.* **117**, 107001 (2016).
- [49] X. Chen, T. Hogan, D. Walkup, W. Zhou, M. Pokharel, M. Yao, W. Tian, T. Z. Ward, Y. Zhao, D. Parshall *et al.*, Influence of electron doping on the ground state of $(\text{Sr}_{1-x}\text{La}_x)_2\text{IrO}_4$, *Phys. Rev. B* **92**, 075125 (2015).
- [50] X. Chen, J. L. Schmehl, Z. Islam, Z. Porter, E. Zoghlin, K. Finkelstein, J. P. Ruff, and S. D. Wilson, Unidirectional spin density wave state in metallic $(\text{Sr}_{1-x}\text{La}_x)_2\text{IrO}_4$, *Nat. Commun.* **9**, 103 (2018).

- [51] M. Ge, T. F. Qi, O. B. Korneta, D. E. De Long, P. Schlottmann, W. P. Crummett, and G. Cao, Lattice-driven magnetoresistivity and metal-insulator transition in single-layered iridates, *Phys. Rev. B* **84**, 100402(R) (2011).
- [52] J. Bertinshaw, Y. Kim, G. Khaliullin, and B. Kim, Square lattice iridates, *Annu. Rev. Condens. Matter Phys.* **10**, 315 (2019).
- [53] E. Pavarini, Electronic structure calculations with LDA + DMFT, in *Many-Electron Approaches in Physics, Chemistry and Mathematics: A Multidisciplinary View*, edited by V. Bach and L. Delle Site (Springer, Cham, 2014).
- [54] M. E. A. Coury, S. L. Duarev, W. M. C. Foulkes, A. P. Horsfield, P.-W. Ma, and J. S. Spencer, Hubbard-like Hamiltonians for interacting electrons in s , p , and d orbitals, *Phys. Rev. B* **93**, 075101 (2016).
- [55] T. Takayama, A. Matsumoto, G. Jackeli, and H. Takagi, Model analysis of magnetic susceptibility of Sr_2IrO_4 : A two-dimensional $J_{\text{eff}} = \frac{1}{2}$ Heisenberg system with competing interlayer couplings, *Phys. Rev. B* **94**, 224420 (2016).
- [56] V. M. Katukuri, V. Yushankhai, L. Siurakshina, J. van den Brink, L. Hozoi, and I. Rousochatzakis, Mechanism of Basal-Plane Antiferromagnetism in the Spin-Orbit Driven Iridate Ba_2IrO_4 , *Phys. Rev. X* **4**, 021051 (2014).